Final Report, June 30, 2016

Project name: Understanding Water Controls on Shale Gas Mobilization into Fractures

Contract #: (Work Proposal #) ESD14085

PIs: Tetsu K. Tokunaga, Jiamin Wan, Abdullah Cihan,

Reporting period: Oct. 1, 2014 to March 31, 2016

Executive Summary:

The overall objective of this research is to understand and predict the dynamics of water-gas interactions within the regions of unconventional shale reservoirs stimulated by water-based hydraulic fracturing fluids (Figure 1). Experimental and modeling research is focused on the manner in which gas recovery is impeded by water imbibed into the shale matrix during stimulation.

Experimental work has primarily been conducted on Woodford Shales, with results including total organic and inorganic carbon (TOC, TIC) analyses, X-ray fluorescence (XRF) elemental analyses, X-ray diffraction (XRD) analyses, scanning electron microscopy (SEM) on thin section samples of shales, water vapor adsorption isotherm measurements, specific surface analyses, gas permeability measurements (crushed shales and cores), and water imbibition rate measurements. TOC values ranged from 2.7% to 7.1% (mass basis). Significant carbonate (TIC = 3.6%) was found in only one sample, Woodford/Holt, which also contained the highest calcium (11.7% mass) and contained identifiable calcite. Quartz and illite are the minerals common to all samples, while calcite was only identified in the high TIC sample. Adsorption isotherms have been completed over wide ranges of relative humidity at both 30 ˚C (0 to 97% RH) and 50 ˚C (0 to 96% RH), on samples from 5 sites. Water desorption isotherms desorption isotherms have also determined for the 50 ˚C condition. Desorption isotherms show significantly higher water contents relative to their levels obtained by adsorption at the same RH, indicative of the importance of water saturation hysteresis in water blocking. Moreover, blocking will persist following hydraulic fracturing until capillary pressures decline to fairly low values. SEM images show complex micromorphology and mineralogy, and are being used to extract pore network information for modeling transport properties.

Several experimental approaches have been used to understand permeability of shales; transient gas pressure pulse in crushed rock, transient water imbibition into shale cores, and steady-state gas probe permeametry. Different aspects of permeability are measured with these approaches, with the crushed rock method best applied to characterize ultra-low permeability characteristic of the grain-scale in some shales, while the gas probe and water imbibition methods being highly sensitive to microfracture networks within shale. We also showed that the crushed rock method generally measures a spectrum of permeabilities rather than a unique value for any given shale. Our imbibition method is well suited for modification for use in imbibition and gas counterflow studies being designed for the next phase of this work.

Modeling efforts resulted in development of a new pore-scale computational model that is based on the many-body dissipative particle dynamics (MDPD). Different modeling approaches for representing pore-scale processes in shale with nanopores were tested. Given the complex and small scale structure of void space in shale rock that might limit the use of traditional

hydrodynamic equations, we decided to follow our theoretical investigations using the MDPD model that is more fundamental and easily applied relative to the others in terms of representing interactions with different minerals and organic matter in rock space, including but not limited to slip flow, wettability, and adsorption and desorption processes. Improvements made on the MDPD model included parallelizing the algorithms for more efficiently conducting simulations with multiple fluids and solid particle types in larger domains. Our computational model was further tested through comparisons with existing numerical and experimental studies. The MDPD pore-scale model was used to simulate imbibition and drainage processes in nanochannels and idealized porous media for testing macroscopic theories of fluid flow. This model will be further improved and used for understanding imbibition and fluid trapping in micromodels and shale rocks during the next phase.

Core-scale modeling studies were also conducted to simulate water imbibition tests in shale rock cores and to test the macroscopic two-phase flow theory with hysteresis in capillary pressure and saturation and relative permeability functions. Macroscopic parameters of the hysteretic constitutive models are linked with the pore-scale properties such as void-size distribution and fluid connectivity functions which are obtained from pore-scale simulations or experimental measurements of primary drainage and main imbibition capillary pressure-saturation functions. Preliminary model results predicting infiltration volumes into shale core were compared against the experimental data. Some discrepancies were observed, but more comprehensive model testing studies will be conducted during the second phase.

In addition to these activities, a preliminary study of methane diffusion and adsorption in shales, in part based on results in our previous reports, was presented by Weijun Shen et al., at the TOUGH Symposium (Berkeley, September 28-30, 2015). Experiments and numerical simulations of water vapor adsorption in shale were be presented by Shen et al. at the American Geophysical Union Fall Meeting (San Francisco, December 14-18, 2015; Shale, mudstone, and clay multiphysics poster session, MR41C-2665).

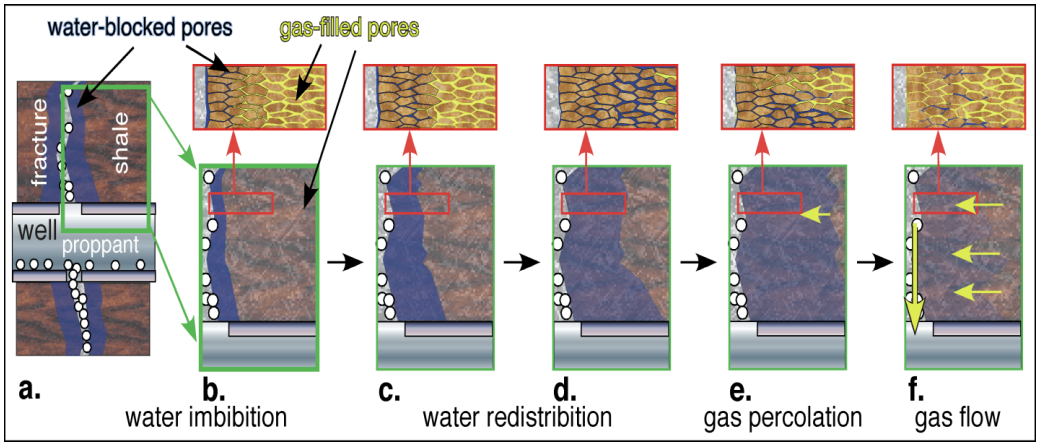

Figure 1. Conceptual model of water-hydrocarbon interactions in unconventional shale reservoirs. a. cross section through horizontal well and new hydraulic fracture, shortly after initial drainage. b. close-up view of water block along fracture, preventing gas/oil flow. c. through f., Redistribution of finite fracturing water volume within shale (spreading while decreasing in average saturation), gas/oil breakthrough across the water block, and increased hydrocarbon flow to well.

Description of Work Performed:

In the following subsections, summaries of specific experimental and modeling activities are provided on shale properties (Task 2) and on water imbibition into shales (Task 3).

Task 2. Shale Properties.

Task 2.1 Shale Properties, characterization experiments: Woodford Shale samples have been our primary test materials because of its importance as a major gas and oil source rock (Cardott, 2012), and because we were able to obtain samples in a timely manner at the beginning of the project. Samples from five different locations within this formation were obtained from the Oklahoma Geological Survey (http://www.ogs.ou.edu/level3-OPICcorefacility.php) (Table 1, Figure 2). Both intact core and rubble samples of Woodford shales were obtained. Our initial laboratory characterization work was done only on rubble. Characterization methods applied to these samples have included elemental analyses (XRF), organic and inorganic carbon analyses, mineralogy (XRD), densities, porosities, and specific surface area measurements. For standardizing measurements, some of the rubble samples were crushed to pass an 800 μm sieve, and further sieved to obtain materials in the 800-500 μm, 500-250 μm, and < 250 μm fractions. A separate Woodford rubble sample from the Dunkin well (denoted WD) was crushed in order to collect sufficient shale mass in the 2.8-3.3 mm sieve size fraction for use in a crushed rock permeameter. More recent work has been performed on cores from the Hoffman, Dunkin, and Holt wells.

LBNL#	OGS#	well	sample depth, m	county
WHf	956	Hoffman	4346.3 - 4347.2	Custer, OK
WR	482	Roetzal	2569.0 - 2569.9	Blaine, OK
WD	4599	Dunkin	282.3 - 283.1	Wagoner, OK
WH1	2595	Holt	1126.7 - 1127.6	Okfuskee, OK
WH2	2595	Holt	1128.5 - 1129.4	Okfuskee, OK

Table 1. Woodford Shale samples obtained from the Oklahoma Geological Survey (OGS).

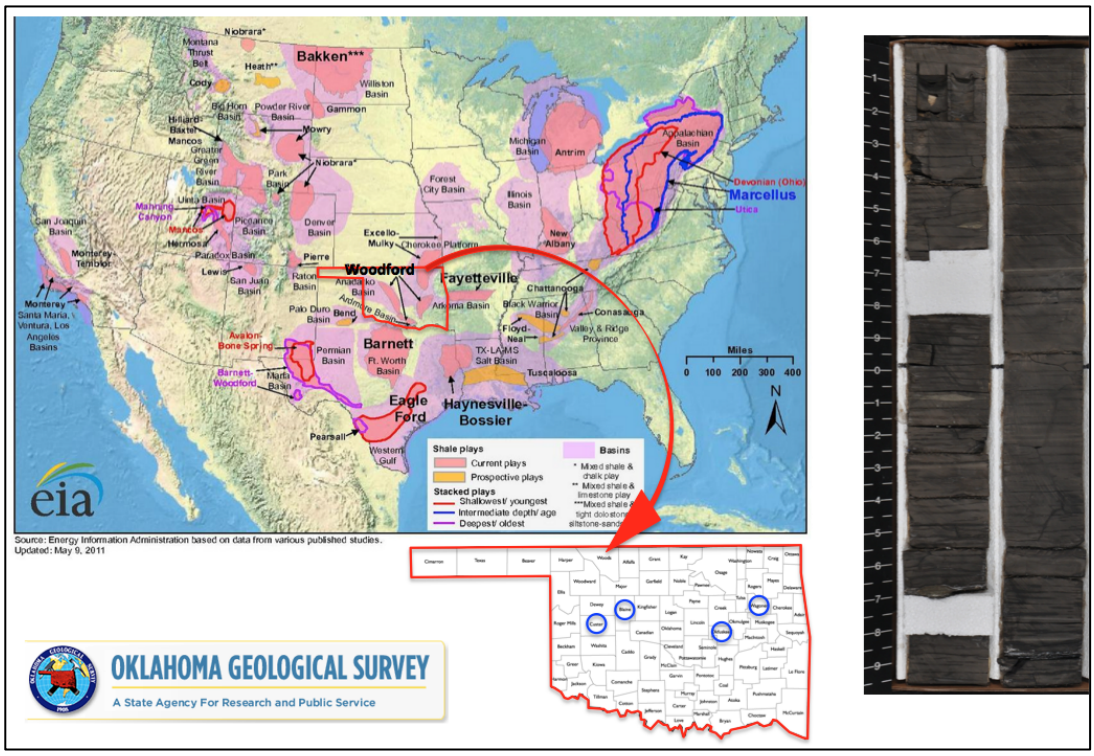

Figure 2. Woodford shales from the Oklahoma Geological Survey (OGS).

2.1.a1. Elemental Composition, Total Organic and Inorganic Carbon

- Elemental composition of the shales was determined by X-ray fluorescence (XRF, Orbis, EDAX) analysis of finely milled (< 10 µm) samples. Total organic carbon (TOC) and total inorganic carbon (TIC) analyses were obtained on the < 250 µm fraction of materials (crushed finer with mortar and pestle prior to analyses) with a Shimadzu TOC-V. These values are reported in Table 2.

LBNL#	Al, %	Si, %	P, %	S, %	K, %	Ca, %	Ti, %	Mn, %	Fe, %		Inorg. C %	Organic C %	major minerals
WHf	9.1	22	0.1	0.3	3.5	1.2	0.4	0.09	3.1		0.40	3.89	q, il
WR	6.6	32	0.1	0.9	3.3	1.0	0.3	0.04	2.0		0.00	7.11	q, il
WD	8.6	30	0.1	0.3	4.3	1.3	0.3	0.03	3.0		0.46	5.61	q, il
WH1	4.8	22	0.1	0.1	1.8	11.7	0.2	0.01	1.0		3.61	2.68	q, il, c
WH2	10	38	0.2	0.2	5.2	2.4	0.5	0.02	2.1		0.00	5.54	q, il

Table 2. Elemental composition of Woodford shales (XRF and TIC/TOC). Major mineralogy determined by XRD; q = quartz, il = illite, c = calcite.

2.1.a2. Mineralogy

- Major mineral composition of the Woodford shale samples was determined by X-ray diffraction (Rigaku Smartlab, CuK_{α} source at 40 kV, 35 mA) using the American Mineralogist Crystal Structure Database [Downs and Hall-Wallace, 2003] . The XRD patterns of the Woodford samples and referenced minerals are shown in Figure 3. Quartz (q) and illite (il) are common in all of our samples. Note that calcite (c) was only detected in the WH1 sample, consistent with our measured total inorganic carbon content of 3.6%.

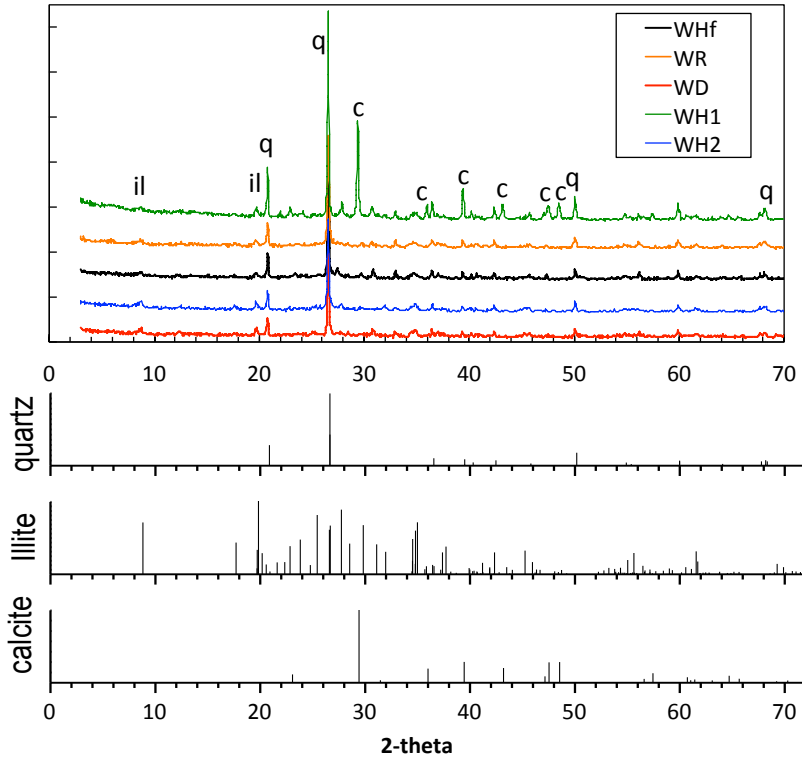

Figure 3. XRD patterns of the Woodford samples and matched reference minerals.

2.1.b. Scanning electron microscopy

The polished thin sections, 30 µm thick and 1" diameter, of the Woodford shale samples were prepared by a commercial petrographic service (Burnham Petrographic, LLC). The thin section surfaces originally contained some volatile organic carbon (organic droplets observed under the light microscope). Therefore, before the gold coating preparation for SEM analyses, the surficial organic droplets were removed using solvent (acetone). The thin sections were sputter coated with a thin layer (10 nm) of gold to increase the surface conductivity. The SEM (Zeiss, Gemini Ultra-55) images were taken with a backscattered electron detector. A few representative images are presented in Figure 4, and the elemental compositions from energy dispersive

spectrometer spot analyses (Figure 5) match with the previously identified dominant minerals; illite, quartz, pyrite, as well as organic/kerogen rich inclusions. The pore sizes vary from tens of nm to µm.

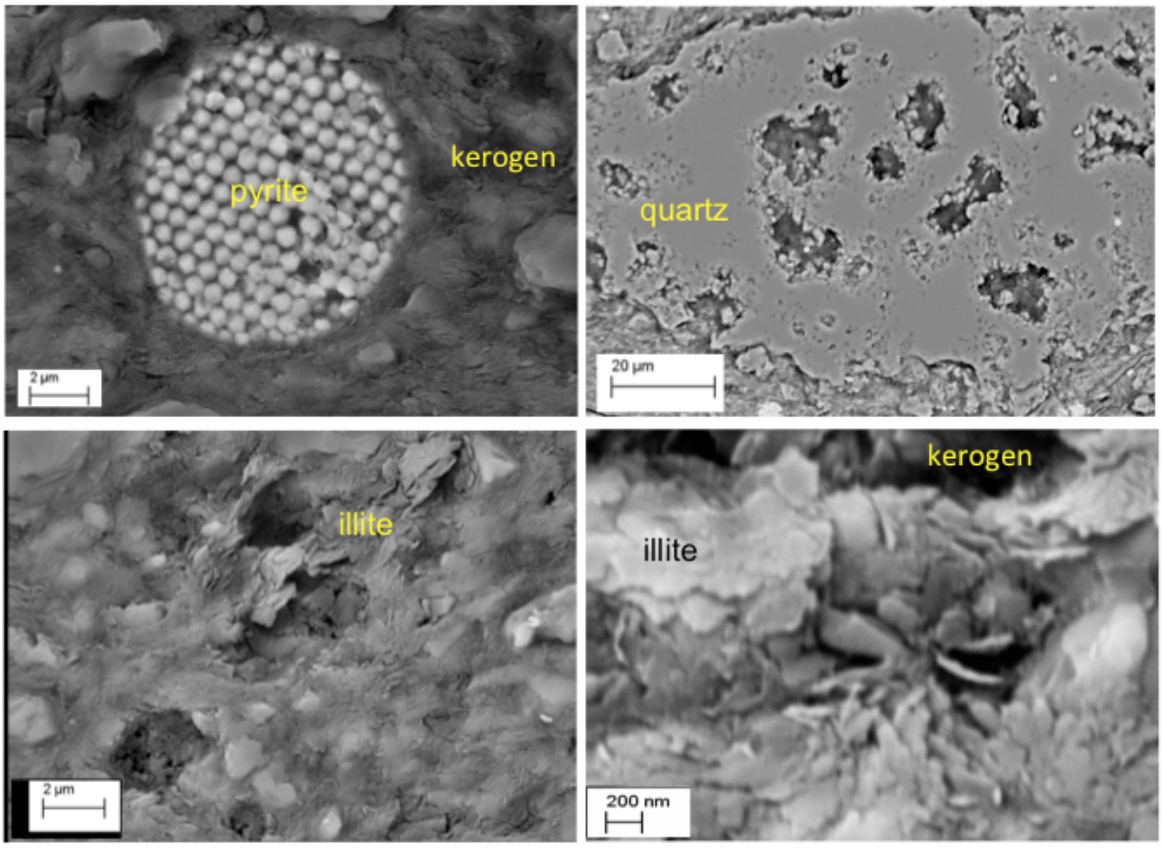

Figure 4. SEM images from characteristic regions in Woodford samples WR and WD.

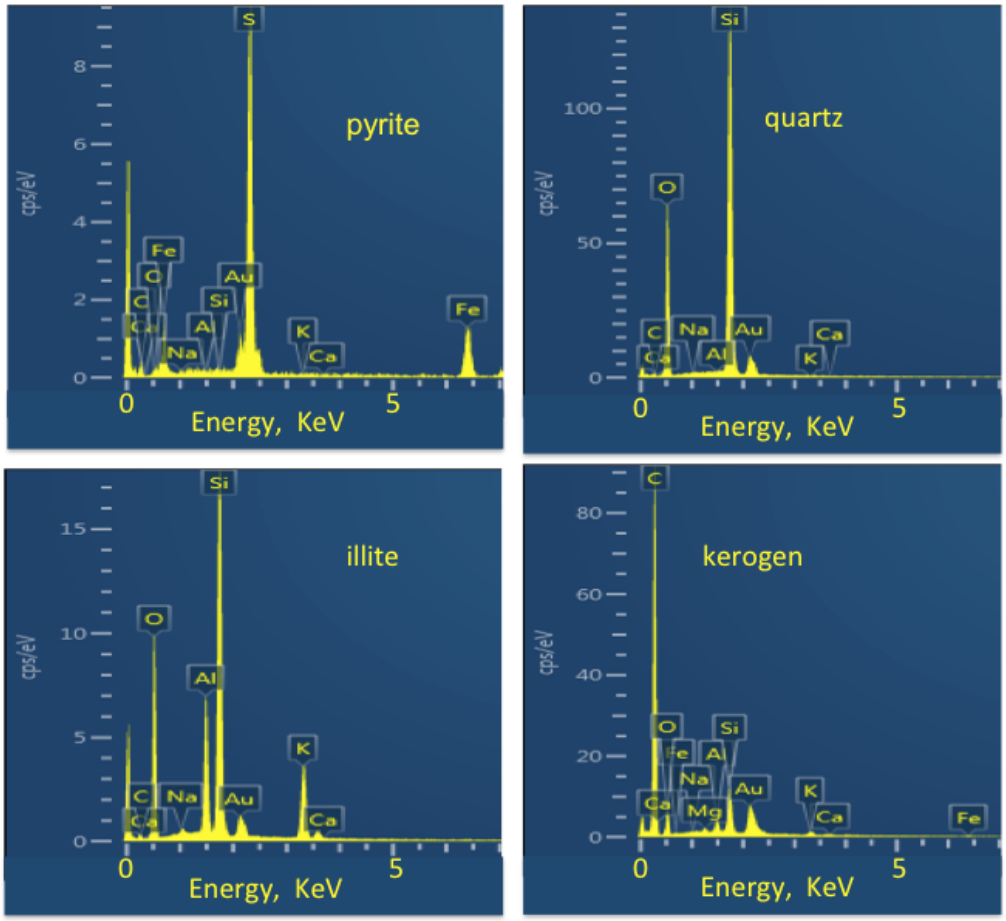

Figure 5. EDS of selected regions from SEM images of Woodford samples WR and WD. Fe- and S-rich pyrite region; Si- and O-rich quartz region; Si-, Al-, O-, K-rich illite region, and C-rich kerogen region (Au in all spectra are from sputter coating).

2.1.c. Specific surface areas.

Specific surface areas of these shales were anticipated to be relatively high, given the measured significant adsorption of water vapor (Figures 6 and 7). Specific surface areas of crushed shale samples were obtained using several different methods. We first used N_2 and Kr gases as the adsorbates in successive applications of the BET method (Brunauer-Emmet-Teller, 1938) using the Autosorb-1 (Quantachrome) in the LBNL Environmental Geochemistry Laboratory. The very low specific surface areas obtain in our laboratory prompted us to send samples out to Particle Technology Labs (Downers Grove, IL), a commercial laboratory that specializes in surface characterization. Their results, listed in Table 3, are compatible with our earlier measurements. With the exception of the calcite-rich WH1 sample, all surface areas obtained with N_2 or Kr BET analyses are quite low, less than 1 m^2/g.

Because such low specific surface areas are unlikely for gas shales, and inconsistent with significant water vapor adsorption, we used the water vapor adsorption data directly to obtain alternate estimates. Applying the BET method with water vapor data (Tokunaga et al., 2003), we obtained specific surface areas more consistent with the measured water uptake, mostly ranging

from 13 to 18 m^2/g, with the WH1 being distinctly lower (~8.6 m^2/g). While these trends are consistent with the water uptake data, they do not constitute independent measurements because they are calculated from the water vapor adsorption results. Moreover, the BET/H_2O analysis is known to over-estimate surface areas in systems where ion hydration is significant (Quirk, 1955). Similar estimates of surface area can be obtained using the Guggenheim- Anderson- de Boer (GAB) method (Anderson, 1946). It is noted that the GAB isotherm has recently been used to describe water vapor adsorption on shales by Dosunmu and Okoro (2012), and by Emmanuel and Dosunmu (2014). The similarities between surface areas obtained with GAB/H_2O and with BET/H_2O are expected because the former is a simple modification of the latter. It should also be noted that specific surface areas of geological materials are not fundamentally unique quantities, but rather measurement method-dependent properties (Sposito, 1984). Thus, the H_2O-based values listed in Table 1 can only represent upper limit estimates of specific surface area.

LBNL#	BET (N2)	BET (Kr)	BET (H2O 30˚C)	BET (H2O 50˚C)	GAB (H2O 30˚C)	GAB (H2O 50˚C)
	m2/g	m2/g	m2/g	m2/g	m2/g	m2/g
WHf	0.21	0.27	13.5	17.5	11.6	13.4
WR	0.24	0.29	15.6	18.4	11.7	13.2
WD	0.31		13.5	15.0	13.6	12.8
WH1	3.03		8.5	8.7	7.3	7.2
WH2	0.91		15.2	17.1	12.7	13.1

Table 3. BET surface areas of Woodford shale samples obtained with N_2 and Kr are from Particle Technology Labs. H_2O-BET surface areas are upper limits based on LBNL water vapor adsorption isotherms.

2.1.d. Water vapor adsorption and desorption isotherms.

These measurements are essential for understanding and predicting water-blocking problems in gas recovery because they provide information on how water saturation (blockage to gas flow) of shale pores depends on the vapor pressure of water (related to water capillary pressure). In order to expedite reaching adsorption and desorption equilibrium while maintaining micropore structure, larger chips of the Woodford samples listed in Table 1 were crushed to grain-size ranges of 500-800 μm and 250-500 μm, denoted as "a" and "b", respectively. After oven-drying (110 ˚C), samples were equilibrated at progressively higher water vapor pressures in closed chambers. Saturated salt solutions were used to control relative humidities (Greenspan, 1977). The first sets of adsorption isotherm measurements were conducted at 30 ˚C. Generally good agreement was obtained between isotherms from the same original specimen crushed to the two different grain-size ranges, such that they were effectively duplicates. Although the similar adsorption-desorption behavior obtained for the 250-500 μm and 500-800 μm size fractions suggest that hydraulic behavior is fairly insensitive to scale in the sub-mm grain-size range, our

various permeability tests show substantial scale-dependence for larger grains and cores (described in sections 2.1.g,h).

After re-drying the crushed shale samples (105 ˚C, 24 hrs), they were reused to obtain the adsorption isotherms at 50˚C. Results of the completed water vapor adsorption at 30 and 50 ˚C are shown in Figure 6. Comparisons of adsorption isotherms at these two temperatures showed relatively insignificant differences with the exception of the highest relative humidity values ($P/P_o > 0.95$). In view of the substantial similarities and the large amount of time required to complete these measurements, we decided to only run the desorption isotherms at 50 ˚C (foregoing running desorption isotherms at 30 ˚C).

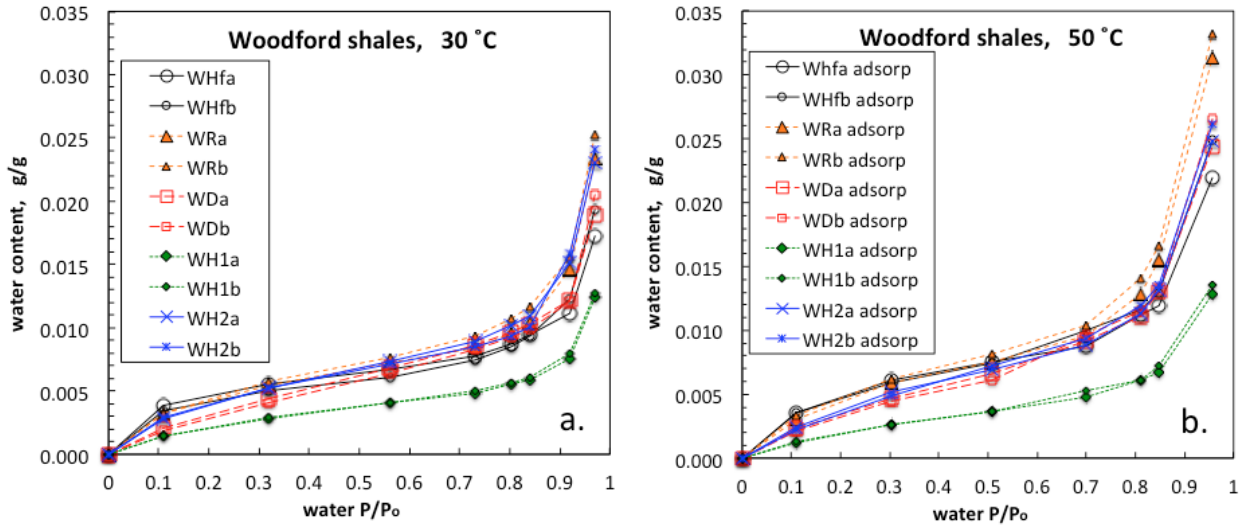

Figure 6. Water vapor adsorption isotherms on Woodford Shale samples, conducted at 30 and 50 ˚C (graphs a and b, respectively). P/P_o is the relative humidity, controlled using saturated salt solutions. The "a" and "b" sample designations denote 500-800 µm and 250-500 µm grain-size ranges, respectively.

After reaching adsorption equilibrium at the highest $P/P_o = 0.96$ at 50 ˚C, samples were sequentially equilibrated at progressively lower P/P_o values in order to determine desorption isotherms. The final adsorption and desorption isotherms are presented in terms of water saturation, based on measurements of densities and porosities. Plots of water saturations within pores of shale grains of two size ranges (500-800 µm and 250-500 µm) as functions of relative humidity are presented in Figure 7. These data clearly show that very high levels of water saturation are achieved at $P/P_o > 0.9$ in most of the samples, show hysteresis characteristic of equilibrium states of water in porous media, and show that substantial decreases in P/P_o are required for removing water from the shale matrix. It is worth noting that these curves mostly show similar magnitudes of moisture retention at any given path-specific P/P_o. The exceptions are associated with the Holt1 (WH1, Figure 7d) samples that have substantially lower water contents. This was the only sample containing significant concentrations of inorganic carbon as calcite (3.61 mass % of C 11.7 mass % Calcium, Table 2), perhaps reflecting less hydrophilic characteristics of carbonate surfaces, as other studies have correlated calcite concentrations with

lower water-wettability of shales (Elgmati et al., 2011; Roychaudhuri et al., 2013). However, this may simply reflect natural variability in organic coatings in view of the fact that WH1 was only about 1 m shallower than WH2 within the Holt well (Table 1). In general, these results indicate that after hydraulic fracturing, water blocking is likely to persist until capillary pressures return to very low levels. However, as shown in sections 2.1h and 3.1, the generally low permeability of the shale allows only fairly shallow imbibition of water into the matrix rock.

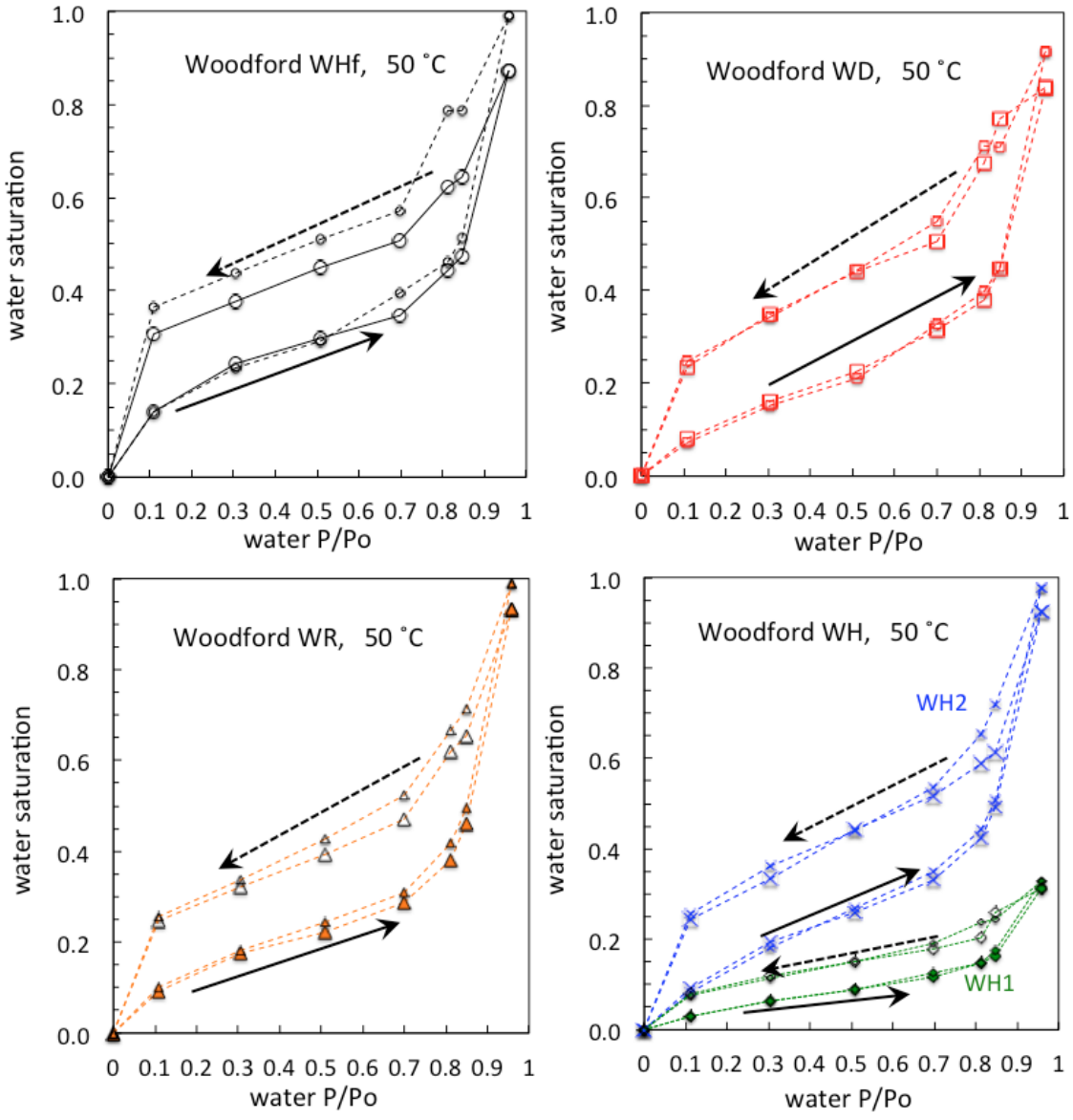

Figure 7. Adsorption and desorption isotherms for Woodford shales at 50 ˚C. Refer to Table 1 for identifying characteristic of the individual samples. **a.** WHf Hoffman, **b.** WR Roetzal, **c.** WD Dunkin, **d.** Holt-1 and Holt-2. Adsorption and desorption paths are indicated with blue and red arrows, respectively.

2.1.f. Crushed rock permeameter.

The very low permeabilities characteristic of shales make conventional core permeability measurements challenging, and motivated the original development of the crushed rock method (Luffel, 1993), and its variants (e.g., Cui et al., 2009; Profice et al., 2012). It is a transient gas pressure pulse method applied to rock grains sieved to a narrow size fraction such that samples can be approximated as collections of equivalent uniform porous spheres. Our system (Figure 8) consists of two small high-pressure vessels (22 cm^3 each, Parr), one containing the crushed shale sample and the other serving as the pressurizing gas reservoir, a high-pressure syringe pump (Isco) for delivering the test gas (usually helium) into the gas reservoir, pressure transducers, and valves. In the most crushed rock permeameters methods, the reservoir pressure is raised while isolated from the sample chamber, followed by opening of the pressurization valve and monitoring decay of the transient pressure increase in the sample chamber. Main components are contained within an incubator that controls experimental temperatures to within ±0.1˚C.

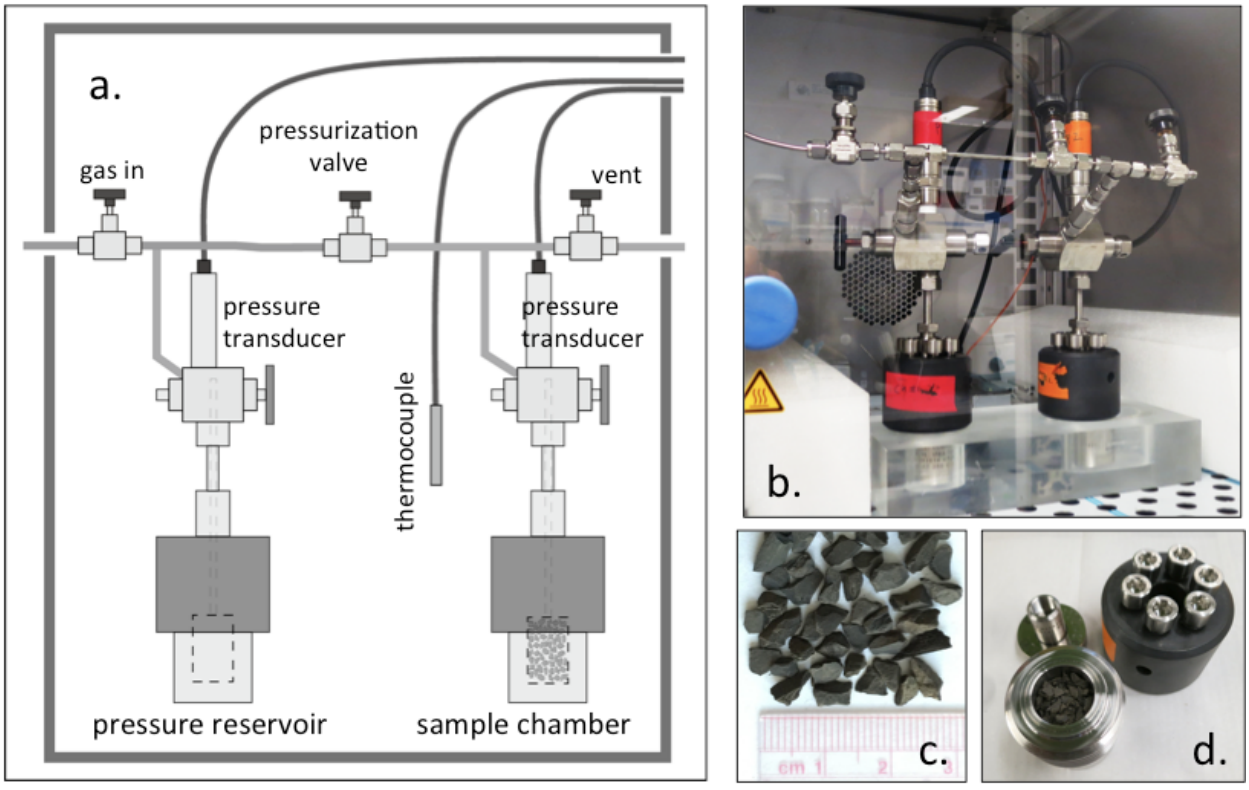

Figure 8. Crushed rock permeameters. **a**. Schematic of modified experimental system. **b**. Photograph of system within temperature-controlled incubator. **c**. Example rock chips (2.8 – 3.3 mm). **d**. opened sample chamber.

We introduced two modifications to this method; (1) a solenoid valve was used as the pressurization valve, allowing quick sample pressurization while not disturbing thermal equilibrium, and (2) instead of leaving the pressurization valve in the open position after pressurizing the sample chamber, we close this valve after the initial step increase. The motivation for the second modification is that it yields greater sensitivity to both porosity and permeability measurements because the effective reservoir volume now becomes the sample chamber volume minus the bulk volume of the crushed shale, eliminating the much larger dead volume of the pressure reservoir. While both of these modifications are in principle advantageous, the solenoid valve had a tendency to slowly leak despite numerous repair attempts. Thus, we switched back to a manual valve, while retaining the second modification of valve closure after initial opening. It should be noted that slow leaks of helium gas are only detectable in long-term (days) permeameters runs needed in analyses of very low permeability (sub-nanodarcy) media, and are challenging to repair in valved systems.

An example measurement of the Woodford Dunkin shale (2.8 to 3.3 mm chips) permeability with He gas, 50 ˚C, initial shale water saturation ~20%, P = 12.78 bar, and time-zero P = 40.11 bar, is shown in Figure 9. Here, the data (points) are compared with analytical solution fits (selected from the series, up to 20 terms). The same data were fit in two different time regions, < 100 s (Fig. 9a), and > 1,000 s (Fig 9b), with permeabilities of ~3.5×10^{-2} and ~10^{-2} nanodarcy, respectively (both with estimated slip corrections). In addition to these estimated permeabilities, gas phase porosity is obtained with this technique because the system is effectively a gas pycnometer when considering initial and final pressures. For this sample, the gas porosity was determined to be 0.033, significantly less than the expected value of 0.056 (with 20% water saturation, only 80% of the estimated total porosity of 0.070 is expected to be gas-filled). Nevertheless, the very low permeability values are consistent with such low porosity as well as low N_2-BET specific surface areas reported previously (Table 3).

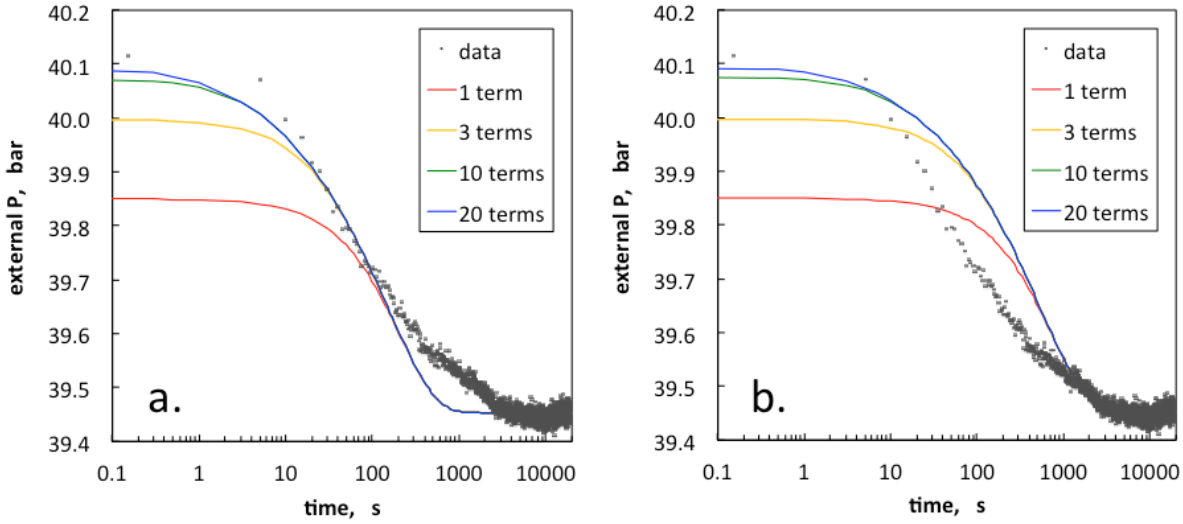

Figure 9. Example pressure response obtained with the crushed rock permeameter using helium gas, 50˚C, initial shale P = 12.78 bar, and time-zero P = 40.11 bar. The same data were fit in the short time region, < 100 s (Fig. 9a), and long-time region, > 1,000 s (Fig 9b), yielding permeabilities of ~3.5×10^{-2} and ~10^{-2} nanodarcy, respectively (both with estimated slip corrections).

Interpreting crushed rock permeameter response curves. We are beginning to explore explanations for the lack of satisfactory matching of data with the simple analytical solution. Real grains of crushed shale deviate from the simple model assumptions in two key ways, geometry and permeability distributions. The model assumes the sample is comprised of identical diameter spherical grains, while crushed shale samples are inherently angular and span a finite size range (Figure 8c). In addition to this basic geometric complexity, permeability among grains and within grains are likely to span a finite range. Both the geometric and permeability variations can be expected to yield response curves that initially decay more rapidly, and later decay more slowly relative to the uniform sphere model. These deviations are not unique to the Woodford Shale. Indeed, most of the data in the original report of Luffel (1993) exhibit these deviations.

2.1.g. Rationale for exploring alternative permeability measurement methods.

The typically very low permeabilities, k, characteristic of the matrix of Woodford shales motivated our use of the crushed rock method (Luffel, 1993; Cui et al., 2009; Profice et al., 2012). With this approach, we obtained k lower than 1 nanodarcy (10^{-21} m^2) on the 2.8 to 3.3 mm size fraction of Woodford shale (WD). However, as shown in our annual report, ambiguities in matching the experimental pressure decay response to the analytical solution can be significant. Moreover, the method assumes that matrix k are scale-invariant so that measurements on rock fragments with sizes in the mm range are representative of flow at the core-scale (> cm). Although studies on some rocks support this assumption (Luffel, 1993; Suarez-Rivera et al., 2012), others report that crushed rock k are generally low than values obtained on cores (e.g., Carles et al., 2007; Ghanizadeh et al., 2015). Thus, we decided to examine other approaches for measuring k. Because of the brittle and weak nature of our shales, and the generally irregular shape of the core samples (deviating from cylindrical symmetry because of chipping and fracturing), we selected methods that required minimal handling. The methods tested are (1) gas probe permeametry, and (2) water imbibition. Of the five Woodford shale samples, only three cores (WR, WD, and WH1) remained intact for these measurements. The gas probe permeameter work is described next, while the imbibition tests are presented in Section 3.

2.1.h. Gas probe permeametry.

The steady-state gas probe permeameter method developed by Goggins et al. (1988) was employed for these measurements. Briefly, the procedure involves imposing a steady flow of gas through a central circular section on one end of the core, monitoring combinations of steady-state flows and associated gas pressures, and employing corrections for flow divergence (specific to dimensions of the source and core) and Klinkenberg slip flow. In our tests, the gas injection source is sealed onto one end of a core with a flat O-ring gasket and quick-setting epoxy, with the probe source secured onto the core with a clamp. The lower limit resolution of k with our system was determined to be ~0.5 μDarcy, based on repeated measurements on a solid acrylic plastic block. The basic experimental system is illustrated in Figure 10a, and results obtained on the three Woodford shale cores are shown in Figures 10b-d. This plots show apparent k (not slip-corrected) as functions of inlet pressure relative to outlet (atmospheric) pressure. The sequence of measurements obtained on the WR sample (Figure 10b) shows an increase in permeability apparently caused by microfracturing of the core during securing of the O-ring probe tip seal for

the second run. The high permeability, ~0.6 mDarcy, obtained on the WD core (Figure 10c) reflects the influence of a through-going fracture.

The experimental sequence shown in Figure 10d illustrates the impact of short term (1 hour) wetting on gas permeability reduction. It should be noted that because of the low water permeability of the shale matrix (estimated at $1x10^{-22}$ m^2, 0.1 nDarcy) the imbibition front only advanced ~ 0.9 mm into the matrix of this shale during the 1 hour wetting period. Systematic tests of water blocking and gas counterflow are to be conducted during the second phase of our project.

The measured apparent k values obtained with the probe permeameter were converted into intrinsic k_∞ using Jones' correlation between k_∞ and the Klinkenberg slip factor b (Jones, 1987). It should be noted that other compilations of permeabilities have yielded very similar correlations for b (Tanikawa and Shimamoto, 2009). The apparent k, k_∞, and b for these cores are summarized in Table 4.

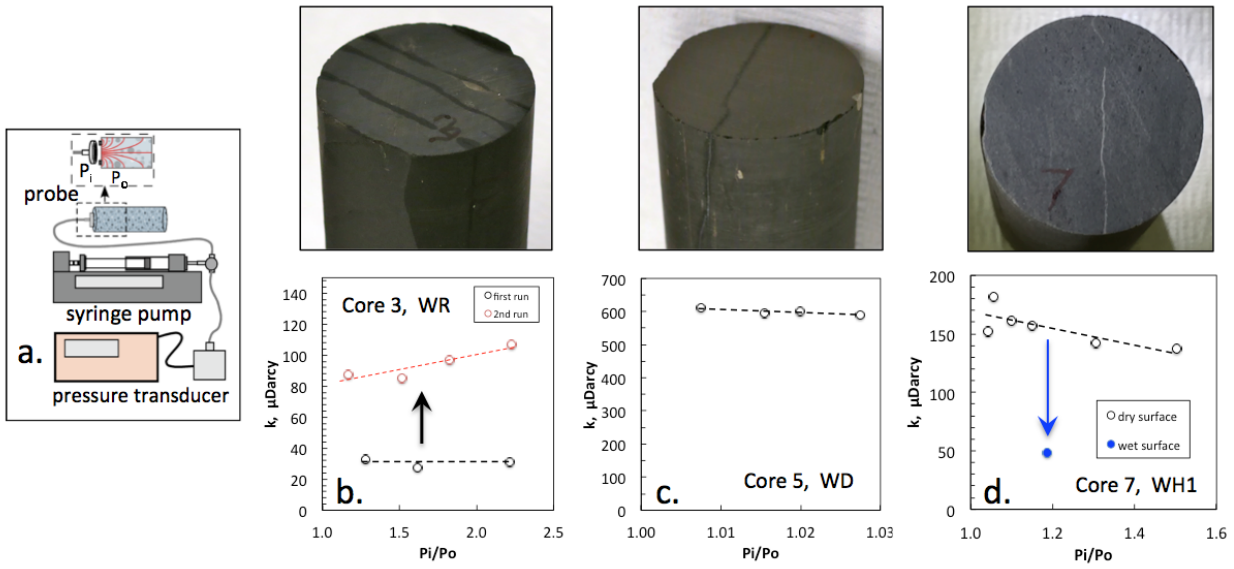

Figure 10. Gas probe permeameter. (a.) basic system components, and apparent k obtained on the b. WR core (showing k increase during the second series of measurements, apparently from microfracturing), c. WD core, and d. WH1 core (showing effecting gas k reduction from wetting) cores.

Although the water imbibition measurements are presented in Section 3.1, we will summarize their implications for permeabilities here. Both the water imbibition and gas probe methods yielded higher values of k than the crushed rock method. The comparisons between measurements summarized in Table 4 further show much higher k (by up to ~ 10^4x) obtained with the gas probe relative to the water imbibition method. Factors contributing to these large differences include preferential gas flow through microfractures, high sensitivity of the water imbibition method to decreases in wettability (Tokunaga and Wan, 2001), intermediate wetting of these organic rich gas shales (Figure 11), and lower impact of microfractures in measurements

based on crushed rock methods. Recent publications have addressed the method-specific nature of permeabilities in shales (Roychaudhuri et al., 2013; Ghanizadeh et al., 2015). Because some of our cores have been damaged in the course of testing, remaining usable segments have been machined in preparation for tests to be conducted under high confining pressures.

method	shale sample	#3, WR	#5, WD	#7, WH1
pycnometry	porosity	0.081	0.070	0.100
water imbibition	S, m/(sqrt(s))	1.5E-06	4.5E-06	1.4E-06
	k(estimated), m^2	4E-22	5E-20	1E-22
air probe	P, Pa	1.7E+05	1.02E+05	1.3E+05
	k(apparent), m^2	3.0E-17	6.0E-16	1.5E-16
	k_∞, m^2	4E-18	2E-16	4E-17
	b, Pa	1.1E+06	2.2E+05	4.3E+05

Table 4. Comparison of measurements obtained on Woodford shale cores via water imbibition and air probe permeametry.

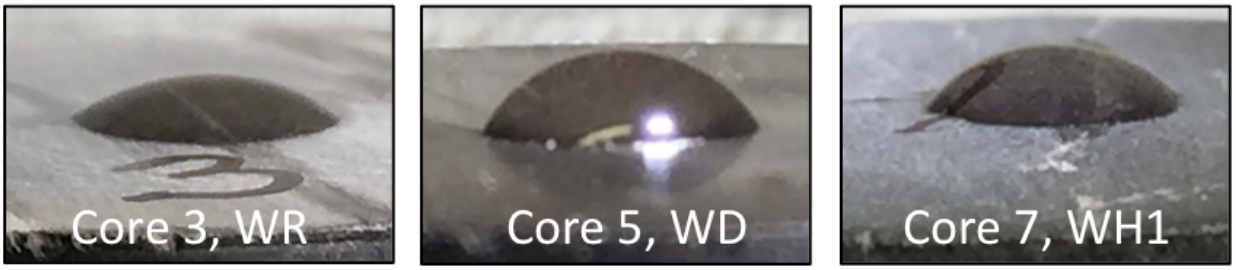

Figure 11. Water droplets on Woodford shale surfaces yielded contact angles ranging from 15˚ to 60˚.

Task 2.2 Shale Properties Model Development

2.2a. Pore-scale modeling:

During Year 1, a pore-scale model was developed, tested, and applied for understanding imbibition in nanoporous media and shale matrix. Our new pore-scale model is based on many-body dissipative particle dynamics (MDPD) method (Hoogerbrugge and Koelman, 1992; Warren, 2003; Ghoufi et al., 2013). As a coarse-grained version of molecular dynamics (MD) method, in MDPD a system is represented by a set of interacting particles and each particle represents a cluster of atoms or molecules. Since its capability of simulating at larger scales compared to MD, the MDPD method is well suited for studying and understanding fluid interactions with different minerals and organic matter in rock space, including but not limited to slip flow, wettability, and adsorption and desorption processes.

According to MDPD, evolution of fluid particles in space and time is governed by Newton's equation of motion:

$$m_i \frac{d\vec{\boldsymbol{v}}_i}{dt} = \sum_{i \neq j} \vec{\boldsymbol{F}}_{ij} + \vec{\boldsymbol{F}}_{ext,i} = \sum_{i \neq j} \left(\vec{\boldsymbol{F}}_{ij}^{C} + \vec{\boldsymbol{F}}_{ij}^{D} + \vec{\boldsymbol{F}}_{ij}^{R} \right) + \vec{\boldsymbol{F}}_{ext,i} \qquad (1)$$

where m_i is the mass and $\boldsymbol{v}_i$ is the velocity with respect to an inertial frame for the ith particle. $\vec{\boldsymbol{F}}_{ij}$ represents the inter-particle forces representing interactions among fluids and fluid-solid particles, and $\vec{\boldsymbol{F}}_{ext,i}$ represents external forces acting on the ith particle. The inter-particle forces involve conservative forces, dissipative (drag) forces and random forces due to thermal fluctuations. In MDPD scheme, a description of the conservative force proposed by Warren (2003) including attraction and repulsion force potentials is employed. Dissipative forces and random forces are described based on Espanol and Warren (1995), Groot and Warren (1997) and Marsh et al. (1997). Espanol and Warren (1995) presents appropriate relationships between random force parameters and drag force parameters to recover proper thermodynamic equilibrium for a MDPD fluid at a prescribed temperature based on the fluctuation dissipation relationship (a derivation is given based on the Liouville and Fokker-Planck equations).

The MDPD-based model can reproduce thermodynamic properties of real systems (e.g., interfacial tension, density, viscosity, compressibility). Force parameters are typically obtained by matching model- calculated thermodynamic properties with measured values, although there are some explicit relationships available derived from statistical mechanical methods to describe the relationships among force parameters and the fluid properties. It is crucial to verify that the fluid dynamic behavior of system of particles is adequately represented by coarse-graining level of choice. Arienti et al. (2011) showed that MDPD is scale-free under a scaling that preserves the physical quantities of interest by following the approach proposed earlier for dissipative particle dynamics (DPD) by Fuchslin et al. (2009). According to this approach, force parameters (measured or obtained at a smaller scale) can be scaled as a function of the number of particles in the coarser system.

We developed a computer program for computation of MDPD simulations with multiple fluids and solid particle types. The system in Eq. (1) is numerically integrated using the velocity-Verley

algorithm to determine evolution of particles in space and time. We examined the sensitivity of different interaction potential (or force) parameters on fluid-solid system behavior and tested of the model and the computer code by reproducing some existing results for simple geometry and no-slip conditions at the pore wall. Some examples of these sensitivity and test simulations are presented below.

Representing miscible, immiscible and different wettability conditions using MDPD

Miscibility and different wettability conditions are represented by changing the conservative force components in MDPD scheme based on the following description:

$$\vec{\boldsymbol{F}}_{ij}^{C} = A_{ij} W_c\left(r_{ij}, r_c\right)\hat{\boldsymbol{r}}_{ij} + B_{ij}\left(\bar{\rho}_i + \bar{\rho}_j\right) W_{cd}\left(r_{ij}, r_d\right)\hat{\boldsymbol{r}}_{ij} \tag{2}$$

where A_{ij} is the attraction parameter (<0), and B_{ij} is the repulsive parameter (>0). W represent weighting functions for attractive (first term) and repulsive (second term) force potentials. r_c and r_d are defined as cut off distances beyond which the attractive or repulsive interactions becomes zero when the relative center-to-center distances r_{ij} among the molecules or particles are greater than the cut off distances.

$$\begin{aligned}
&\bar{\rho}_i = \sum_{i \neq j} W_\rho\left(r_{ij}, r_d\right) \\
&W_\rho\left(r_{ij}, r_d\right) = \frac{15}{2\pi r_d^3}\begin{cases}(1 - r_{ij}/r_d)^2 & r_{ij} < r_d \\ 0 & r_{ij} \geq r_d\end{cases},\ r_d = 0.75 \times r_c \text{ (a common choice)} \\
&W_{cd}\left(r_{ij}, r_d\right) = \begin{cases}(1 - r_{ij}/r_d) & r_{ij} < r_d \\ 0 & r_{ij} \geq r_d\end{cases}
\end{aligned} \tag{3}$$

Interaction force parameters (A_{ij}, B_{ij}) can be deduced based on matching interfacial tension and contact angle parameters. The stress tensor is calculated based on the Irving-Kirkwood equation (Irving and Kirkwood, 1950) as a function of particles mass and velocity, thereafter the interfacial tension can be directly calculated for specific fluid-fluid-solid systems. Some examples of these procedures given by Chen et al. (2012) were reproduced here for testing of the computer code and understanding the effect of interaction force parameters in creating different immiscibility and wettability conditions.

In Figure 12, the simulation results with our pore-scale modeling tool are presented in a capillary tube for different wettability conditions. Force coefficient A_{sl} between solid (black) and liquid (blue) (white is vacuum) is varied to create hydrophilic or hydrophobic conditions resulting in different contact angles. Solid or wall particles are represented by following the methodology by Henrich et al. (2007), where solid particles are pinned to their equilibrated positions by a spring force, while they interact with fluid particles. By this methodology rough surfaces and complex geometries are easily represented.

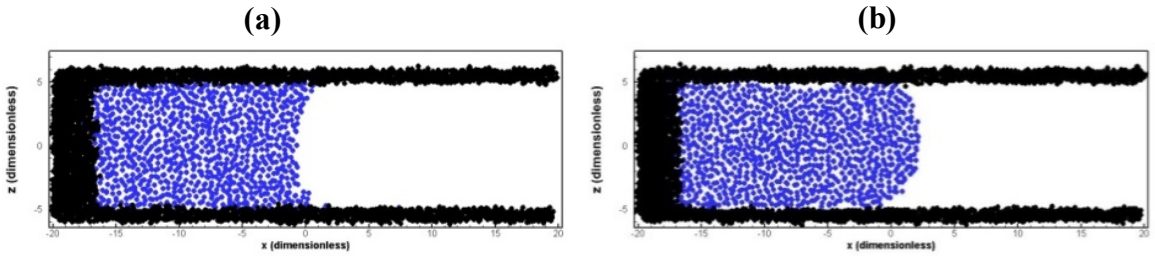

Figure 12. (a) $A_{sl} = -35$, Hydrophilic conditions between fluid and solid (contact angle~40deg) and (b) $A_{sl} = -15$, Hydrophobic conditions between fluid and solid (contact angle~160deg)

Figure 13 shows another example simulation results in a box (with periodic boundary conditions) on creating/representing miscible and partially miscible conditions by varying force parameters. Higher attraction forces results in a miscible behavior, while lower attraction results in immiscibility of the fluids.

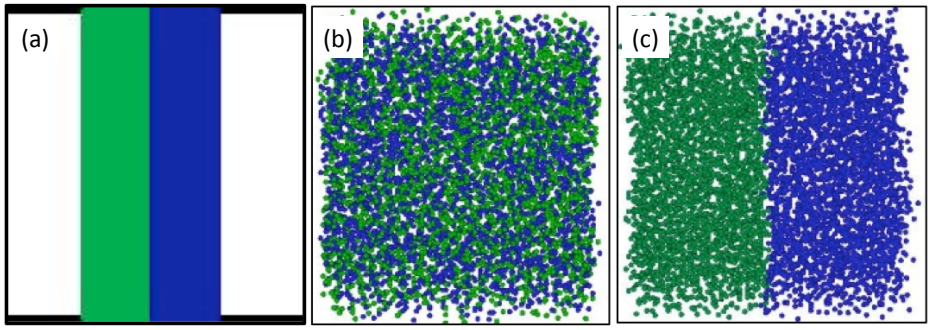

Figure 13. (a) Initial conditions for the simulations, (b) $A_{l-l} = -40$, completely miscible fluids and (c) $A_{l-l} = -25$, immiscible fluids.

We improved our developed computer program by parallelizing the algorithms for more efficiently conducting MDPD simulations with multiple fluids and solid particle types in larger domains. We also continued testing our computational model with the existing numerical and experimental studies. Some examples of the test simulations are presented below.

Single-phase in a capillary tube: Simulating Poiseuille flow in a rectangular domain and comparing against Navier-Stokes solution

The MDPD-based computational model results for single-phase flow were compared against Navier-Stokes solution in rectangular domain. Initially, 17280 homogeneous particles ($\rho = 6$) is injected into a 40x3x12 box with periodic boundary conditions in all the sides, and then the model was run until equilibrium. The particles located at $|z| > 10r_c$ are set as wall particles, and the rest as fluid particles. For representation of the wall, the methodology proposed by Henrich et

al. (2007) is employed. After obtaining the initial conditions, the simulations continued by applying an external force (pressure-gradient) and the time-average velocity computed $v_x(z)$ was calculated as a function of time. Figure 14a shows that the MDPD calculated steady velocity profile almost perfectly matched with the Navier-Stokes solution for steady flow of a homogeneous fluid with no slip boundary conditions.

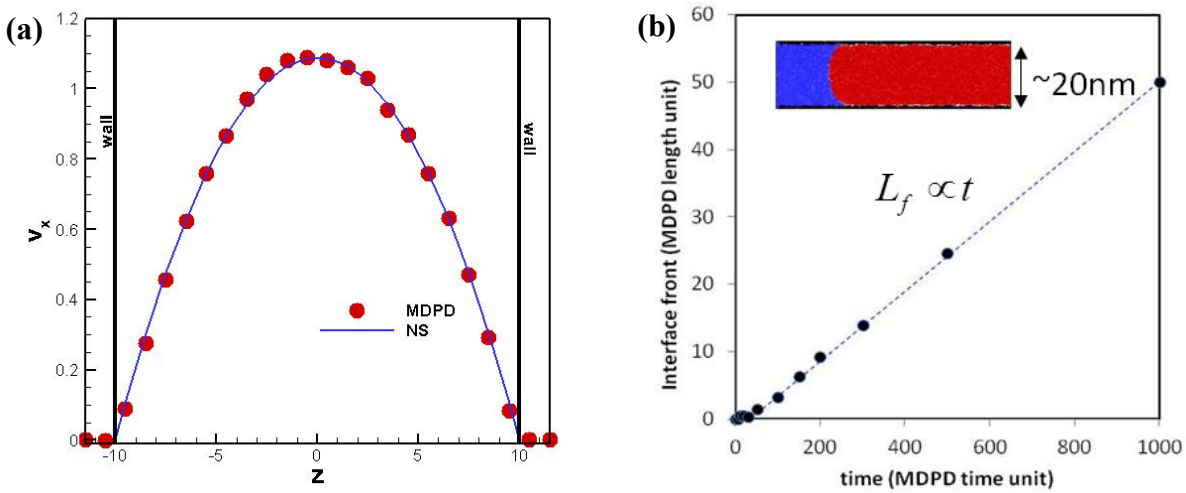

Figure 14. (a) Comparison of the MDPD results with the NS solution results for steady flow under no-flow boundary conditions at the channel walls. (b) Demonstration of the MDPD-predicted results for the interface front movement during the spontaneous imbibition in a nanotube. (Black=solid, blue=wetting fluid, red=nonwetting fluid).

Test simulations for representing two-phase flow in nano-tubes and nonporous media

The MDPD simulations for spontaneous imbibition of a wetting fluid into an initially nonwetting fluid in a nanotube were conducted, and the conformance of our results was checked against the data from the literature obtained from similar systems. The setting of the particles (~48384 heterogeneous particles including two fluids and tube-wall particles) and equilibrium simulations were conducted as similarly to the single-phase phase simulations above. However, in this case, the attractive and repulsive components of the interaction forces between fluid and wall varied for each fluid to create different wettability conditions. Figure 14b shows the distance to the interface from the inlet of the tube as a function of time, measured along an axis passing through the middle of the tube parallel to the walls. It is interesting that the interface front is *not proportional* to the square root of the time, contrary to the Lucas-Washburn (LW) equation prediction, $L \sim t^{1/2}$, in capillary tubes. Similar results were found also by other researchers (e.g., Supple and Quirke, 2004; Cupelli et al., 2008) for partially wetting fluids in nanotubes, attributed to dynamic contact angle and fluid slip not taken into account by LW. This may indicate that, due the action of attractive forces in a shale rock matrix consisting of nanopores, the wetting fluid can imbibe more rapidly than it could be supposed based on the traditional LW equation. Further studies will be conducted to confirm the results for different fluids specific to gas-shale rocks.

We also conducted simulations for the forced drainage and imbibition of fluids. The force is created using a set of piston particles based on the method similarly to the one proposed by Chen et al. (2014) (Figure 15). A threshold pressure (force/area) needs to be exceeded for a nonwetting fluid to enter into the system.

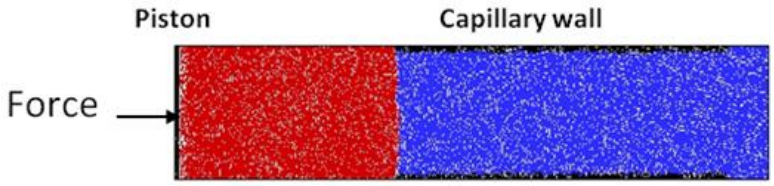

Figure 15. Simulation of forced drainage and imbibition.

Figure 16 also presents a simple demonstration example of a forced imbibition of a wetting fluid into a quasi 2D nano-porous medium. The same type of simulations with water and supercritical methane will be conducted for realistic pore spaces of the shale rock.

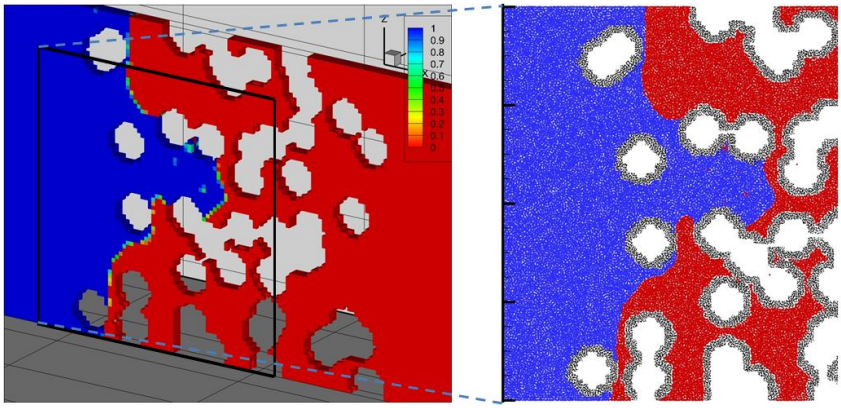

Figure 16. A simple demonstration example of forced imbibition of a wetting fluid into a nano-porous medium (Contour plot on the left shows spatial distribution of a phase indicator function, averaged over the number of particles).

We also developed an algorithm to extract the image data into the MDPD-based pore-scale model. The image can be either computer-generated based on statistical properties or directly obtained from the actual rock samples. An example demonstration of this algorithm and resulting particle distributions for a random sample is shown in Figure 17.

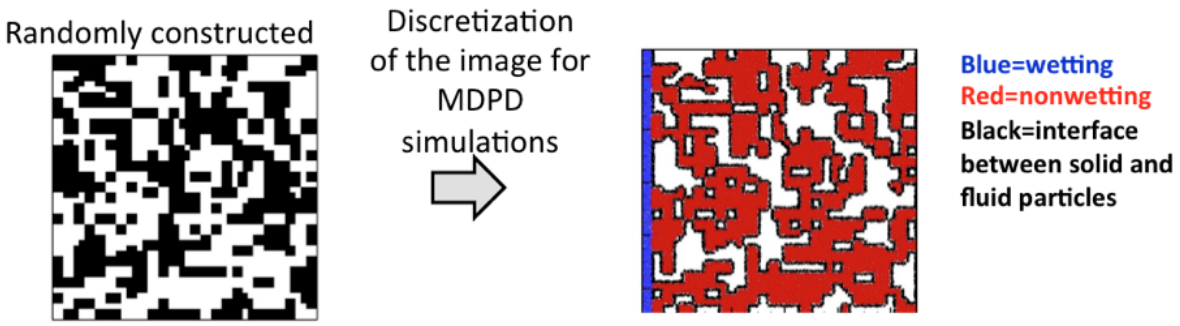

Figure 17. Construction of the MDPD simulation domain based on the images. Only the thin interface of the solid phase (black) between the solid and fluids are retained for computational efficiency.

2.2b. Macroscopic modeling of multicomponent diffusion and adsorption/desorption

We also worked on macroscopic-scale simulation of adsorption/ desorption experiments for single-phase flow with binary gaseous species transport. The results from these studies will be used to test the models and understand the transport processes in shale rock, comparing against the adsorption/desorption batch experiments with the crushed shale rock samples (subtask 2.1). For modeling of the gas adsorption/desorption and diffusion, we use the Maxwell-Stefan diffusion model. Some preliminary modeling results are presented in Figure 18 for the adsorption of water molecules on the solid phase, where a single grain of the crushed rock sample with nanopores is represented a sphere. The Maxwell-Stefan equations are solved for different boundary conditions of RH described at all sides of the box outside of the spherical grain. We are currently in the process of interpretation of the permeability test using the models including Knudsen diffusion. The pore-scale model will be used to generate the macroscopic model parameters at a grain-scale. Comparison of the measured and the predicted adsorbed mass changes and the equilibration times will inform pore-space connectivity and contribution of diffusive processes, particularly Knudsen diffusion.

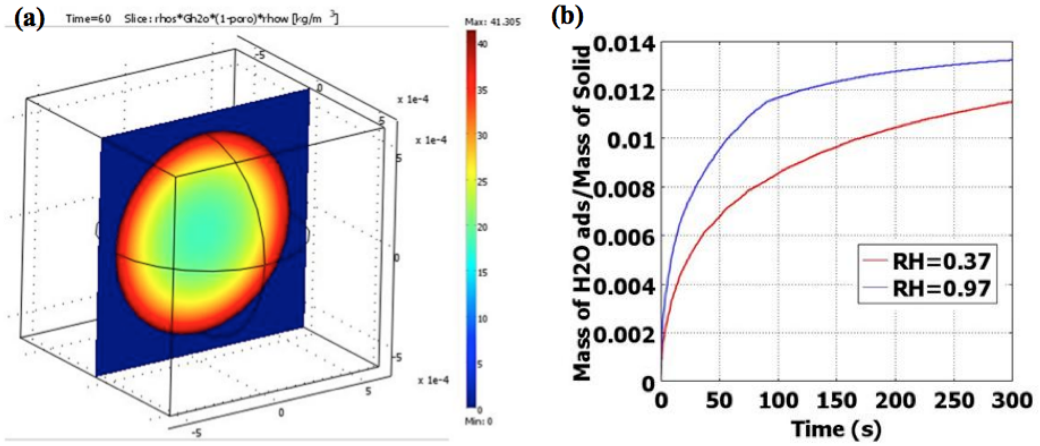

Figure 18. Preliminary macroscopic modeling results at a grain-scale. (a) A snapshot of adsorbed H_2O concentration at t=60 s, initially H_2O vapor concentration=0. (b) Changes in the ratio of the adsorbed mass to the mass of the solid as a function of time under different RH conditions.

Task 3. Understanding and predicting imbibition and redistribution

Progress on our experimental and theoretical studies of water imbibition and redistribution is summarized in the following sections. These initial investigations provide the background for more complex studies to be conducted in the next phase of this work.

3.1. Water imbibition laboratory tests.

The water imbibition experiments served multiple purposes. Most generally, the experiments simulated fracturing fluid interactions with the shale matrix, and thus gas flow measurements before and after water exposure permit examination of formation damage associated with water-blocking (e.g., Figure 10d). This key aspect of water impacts is the focus of our next phase of research. In the first phase of this project, the main application of imbibition experiments was as an alternate method for characterizing shale permeabilities.

We selected water imbibition as one of the alternate methods for estimating *k* because it imparts minimal mechanical stress on the relatively fragile cores, and it simulates one of the main processes of interest, hydraulic fracturing fluid absorption into shale. A schematic of the basic procedure is shown in Figure 19a, where a vertically-oriented core imbibes water from a horizontally-oriented pipette. A permeable microporous membrane at the base of the core allows supply of water at a finite capillary pressure. The horizontal orientation of the pipette (Figures 19a,b) allows inflow of water while maintaining constant capillary pressure. The inflow water consisted of 0.50 molal $CaCl_2$, with its high ionic strength (1.5 molal) used to minimize clay swelling (the electric double layer effective Debye length ~ 0.25 nm with this electrolyte solution). Water uptake is most rapid initially when the hydraulic gradient is highest and gradually declines over time (Figure 19c), with the time dependence scaling closely with the square-root of time (Figure 19d), as has been long established for both capillary tubes and porous media (Bell and Cameron, 1906; Green and Ampt, 1911; Lucas, 1918; Washburn, 1921). It is important to remember the limitation of wetting front propagation in low *k* media, that wetting is restricted to very shallow depths over moderate times. For example, the case shown in Figure 19c with cumulative infiltration of 0.15 mm after 3.5 hours amounts to a wetted distance of only about 2 mm (porosity = 0.070). Thus water blocking in tight shales can be localized within very thin envelopes bounding newly formed fractures.

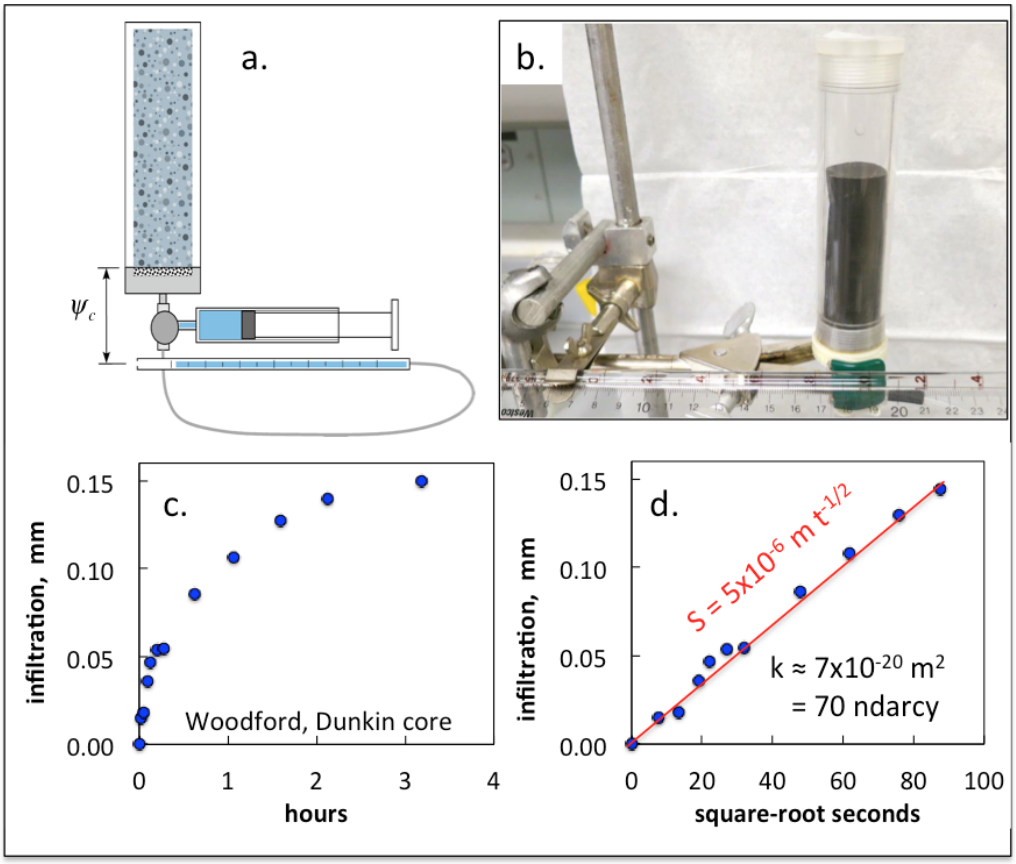

Figure 19. Core permeability from imbibition measurements. **a**. Schematic of imbibition measurement system showing inflow from bottom of core at a fixed capillary pressure, with cumulative inflow measured via horizontal pipette (refill syringe is isolated during measurements). **b**. Photograph of system in operation (room temperature run, plastic sleeve over core to prevent evaporation). **c**. Cumulative water infiltration (water volume imbibed per inlet area) versus time. **d**. A plot of infiltration versus square-root of time yields the sorptivity *S*, and estimated permeability through Equation 4.

The proportionality constant for square-root of time imbibition (Figure 2d) is the sorptivity *S* (Philip, 1957). Based on this behavior for water uptake and a similar time-dependence for the movement of the wetting front (Kao and Hunt, 1996), we obtained a correlation between *S* and *k* (Tokunaga and Wan, 2001),

$$k \approx \left(\frac{\mu}{\sigma}\right)^2 \left(\frac{S}{B\Delta\theta}\right)^4 \tag{4a}$$

where μ is the imbibing wetting fluid viscosity, σ is the fluid-fluid interfacial tension, $\Delta\theta$ is the change in volumetric water content upon imbibition (step-function approximation), and B ~0.5. For imbibition involving water and air at room temperature, Eq. (4a) becomes

$$k\left[m^2\right] \approx \left(3\times10^{-3} s^2 m^{-2}\right)\left(\frac{S}{\Delta\theta}\right)^4 \tag{4b}$$

Permeabilities of the three Woodford shales estimated from this procedure are all in the nanodarcy range, and summarized in Table 4. The imbibition time trends for these shales were used in part of the model testing described in section 3.2.

3.2 Imbibition and Redistribution Modeling

We conducted test simulations for imbibition of multiple fluids in nanochannels and porous media. We have used the MDPD simulations and macroscopic models to understand the nature of imbibition and fluid entrapment in shale rock matrix. The MDPD simulations were conducted in nanochannels of various sizes ranging from 2nm-20nm. The interface front in nano-scale channels appeared to be proportional to the time, rather than the square root of the time at least relatively early times, contrary to the Lucas-Washburn (LW) equation prediction, $L \sim t^{1/2}$, in capillary tubes based on Poiseuille's equation (Figure 20). Similar results were found also by other researchers (e.g., Supple and Quirke, 2004; Cupelli et al., 2008) for partially wetting fluids in nanotubes, attributed to dynamic contact angle and fluid slip not taken into account by LW. This indicates more rapid movement of water in nanoscale channels than in larger-scale capillary tubes predicted by the standard theory based on the Lucas-Washburn equation. However, all of these studies including those we obtained were conducted in relatively short travel length distances and times, and therefore, to be more conclusive about the deviation from the standard theory, we will be conducting the MDPD simulations for longer channels and time periods. We are also currently testing if the same phenomena occur in actual porous media with different grain sizes and different initial water saturations. Strong interactions between water in nanopores and rock material at microscopic scales might be partially responsible for the observations of rapid and significant water loss at field-scale applications of the hydraulic fracturing.

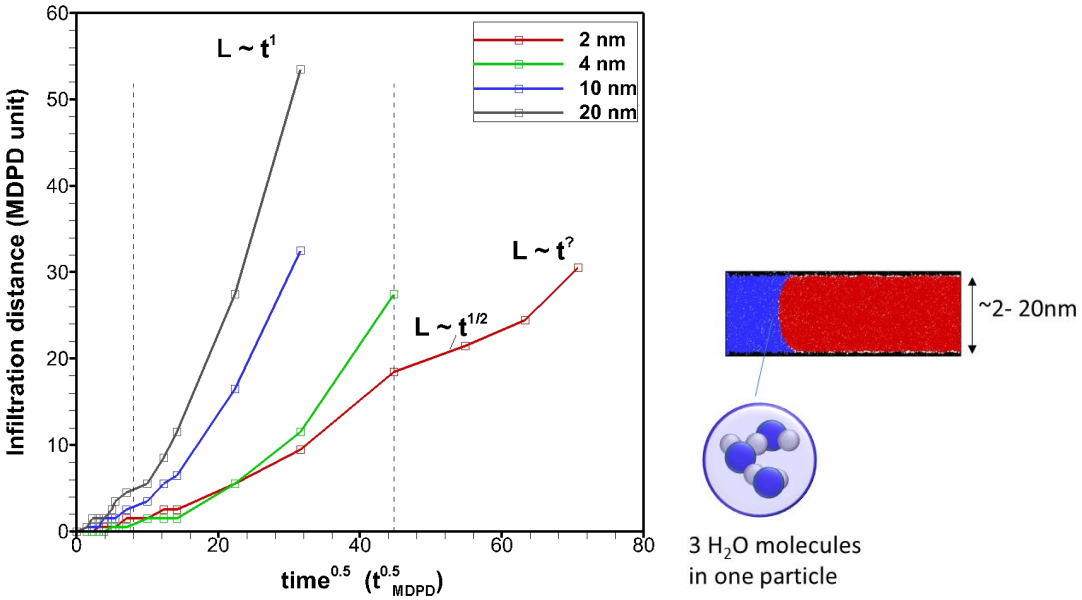

Figure 20. MDPD simulation results for the interface movement as functions of time and nanochannel size under two-phase flow conditions. 1 MDPD particle of the wetting fluid phase corresponds to 3 water molecules (6400 MDPD time unit ~ 1 microsecond and 60 MDPD length unit ~ 60 nm).

During in Phase I, we also started employing macroscopic models to test theories and evaluate imbibition, redistribution and trapping. We simulated some of the water imbibition tests in section 3.1 using the traditional two-phase flow theory with hysteresis in capillary pressure and saturation and relative permeability functions. Hysteresis in the macroscopic model of the traditional theory is hypothesized to be crucial for predicting redistribution and entrapment following the water imbibition. The hysteretic constitutive models are based on Cihan et al (2014a-b) and require some knowledge of void-size distribution and fluid connectivity functions during drainage and imbibition. We generated arbitrarily a probability distribution function (pdf) for volumetric ratios of varying void sizes based on the literature and the adsorption tests (Figure 21). Then, based on the pdf and some representative connectivity functions for the rocks, we estimated capillary pressure – saturation and relative permeability functions (Figure 22), which were used for simulating two-phase flow in shale rock cores. These are very initial estimates and from these rough estimates, the model predicted infiltration volumes for a range of intrinsic permeability values were compared against the experimental data (Figure 23). The model results are promising, but more comprehensive model testing studies will be conducted in the future. The fact that the data fall below the modeled curves in Figure 23 shows that the effective water permeability of the core is at a nano-darcy range.

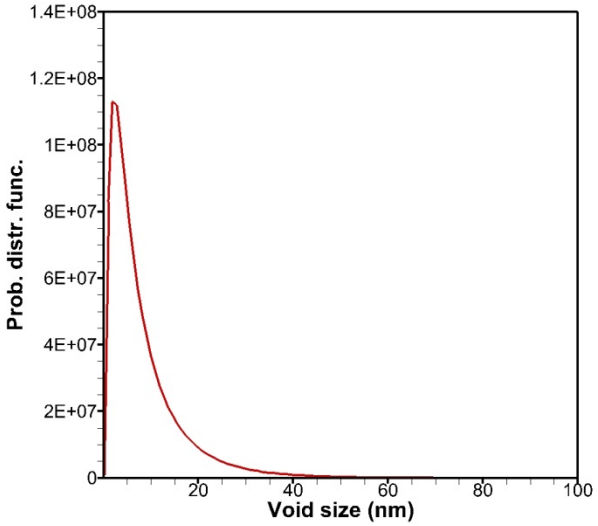

Figure 21. The assumed probability distribution function for void volume fraction of varying void sizes for pores in shale rock matrix.

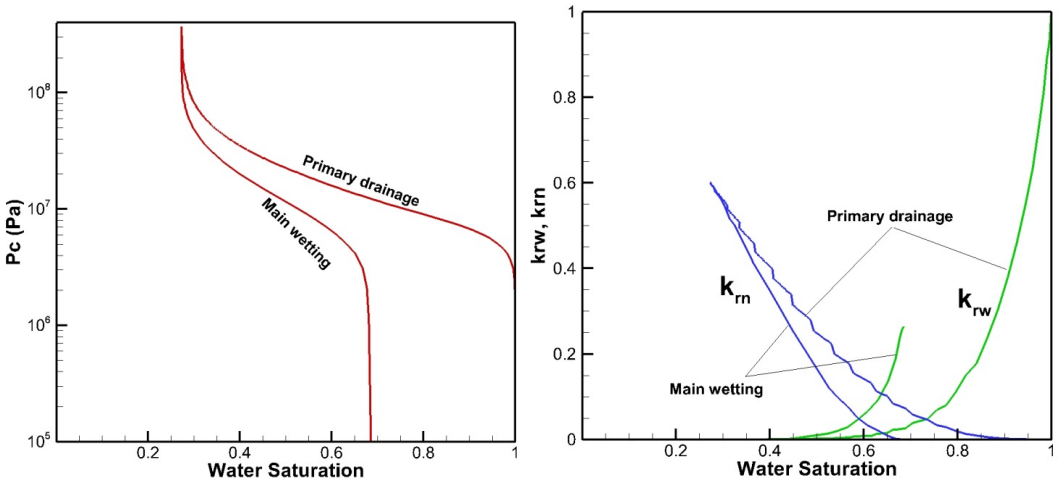

Figure 22. The generated primary drainage and main wetting Pc-S and relative permeability functions for the shale rock matrix.

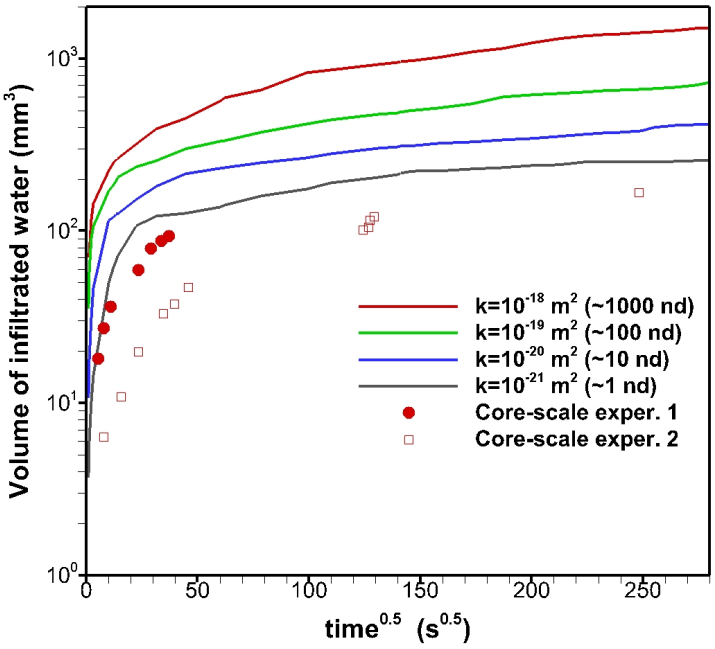

Figure 23. Preliminary modeling results for water infiltration into shale rock cores.

Research Needs and Outline of Second Phase Plans

These initial experimental and modeling studies show both the importance and complexity of the water-blocking phenomenon in unconventional reservoir development. The water imbibition substantially reduces gas permeability of the shale matrix while penetrating relatively short distances from fractures. Very strong capillary forces associated with water imbibed into very fine pores limits rates of water block redistribution, dissipation and eventual gas breakthrough. Indeed, the nanoscale range of pore sizes with variable wettability make even the quantification

of specific surface area highly procedure-dependent. While we identified the importance of longer-term evolution of water redistribution in the shale matrix on gas production and have developed experimental and theoretical/computational methods for addressing this problem, this key issue remains to be systematically investigated.

On the experimental side, the next phase of research focuses on two basic needs. The first need is to investigate later stage water redistribution in shales and relations with return flow of gas. Building on our recent NETL-supported work on shales and on years of experiments related to geological carbon sequestration, these next phase shale experiments will be conducted at elevated pressures and temperatures. The transient water imbibition, redistribution, and gas counterflow experiments on shale cores will provide the first realistic laboratory insights into the multiphase flow dynamics controlling shale matrix-fracture interactions. These experiments will benefit from insights gained from our modeling team, and from X-ray computed tomography to be conducted through collaboration with Dustin Crandall (NETL).

In view of numerous problems associated with water-based stimulation of unconventional reservoirs, the second focus of the experiments will be on non-water stimulation fluids, particularly in oil reservoirs. We again will investigate multiphase flow between hydrocarbon rich matrix blocks and fractures, but here the experiments will be conducted in transparent glass micromodels, with replicated pore geometries for testing different fluid pair interactions. These high presuure pore network experiments build on our decades of experience with micromodel investigations into multiphase flow. As with the planned core-based experimental effort, our modeling team will provide quantitative analyses of the micromodel oil displacement experiments.

Theoretical research during the next phase needs to focus on understanding impacts of pore-scale processes at larger scales of shale, with the ultimate objective of developing predictive macroscopic models to be used for field applications. Both pore-scale and core-scale modeling studies will be conducted during the next phase to compare the model results against experimental data generated from micromodels and core-scale experiments. The tests at different scales will lead to development of new or improved mathematical macroscopic models including the effects of important pore-scale processes to accurately capture the multiphase flow processes in shale.

The pore-scale modeling approach that was developed at the initial stages of the project was shown to have potential to represent multiphase fluid-fluid and fluid-solid interactions in shale matrix. However, we will need to improve the methodology to solve pore-scale multiphase flow problem at large enough scales to investigate macroscopic behavior in shale with nanometer-scale pores. For this objective, we have already developed new computational approaches that are planned to be applied during the next phase of the project.

There is also a need to comprehensively test the applicability of the existing multiphase flow theory with hysteresis effects against core-scale experiments and pore-scale simulations that are planned during the next phase of this research. The macroscopic modeling work was initiated during the earlier phase of the project, but more work needs to be done. Our theoretical research will also continue seeking for new macroscopic modeling approaches to better predict multiphase flow and redistribution in unconventional rocks.

Acknowledgments

Support for this research provided by DOE-NETL and project management by Stephen Henry (NETL) are gratefully acknowledged. We thank the Oklahoma Geological Survey and Dr. Brian Cardott (OGS) for guidance on sample selection and for Woodford formation samples, Weijun Shen for water vapor adsorption isotherm measurements and carbon analyses, and Dr. Yongman Kim for XRD analyses and permeameter construction and operation.

References

Anderson, R. B., (1946), Modifications of the Brunauer, Emmett, and Teller equation, *J. Am. Chem. Soc.* 68, 686-691.

Arienti, M., W. Pan, X. Li, and G. Karniadakis, (2011) Many-body dissipative particle dynamics simulation of liquid/vapor and liquid/solid interactions, *J. Chem. Physics*, 134.

Backer, J. A., C. P. Lowe, H. C. J. Hoefsloot and P. D. Iedema, (2005), Poiseuille Flow to Measure the Viscosity of Particle Model Fluids, *J. Chem. Phys*., 122, 154503

Bell, J.M., and F.K. Cameron (1906), The flow of liquids through capillary spaces, *J. Phys. Chem.*, 10, 658-674.

Cardott, B. J. (2012), Thermal maturity of Woodford Shale gas and oil plays, Oklahoma, USA, *International Journal of Coal Geology*, *103*, 109-119.

Carles, P., P. Egermann, R. Lenormand, and J.M. Lombard (2007), Low permeability measurements using steady-state and transient methods, SCA2007/7, 12 pages, *Society of Core Analysis*, Calgary, September 10-14, 2007.

Chen C., L. Zhuang, X. Li, J. Dong and J. Lu, (2012), A Many-Body Dissipative Particle Dynamics Study of Forced Water–Oil Displacement in Capillary, *Langmuir*, 28, 1330–1336.

Cihan, A., J. Birkholzer, T. H. Illangasekare, and Q. Zhou (2014a), A modeling approach to represent hysteresis in capillary pressure-saturation relationship based on fluid connectivity in void space, *Water Resour. Res*., 50, doi:10.1002/2013WR014280.

Cihan, A., J. Birkholzer, L. Trevisan, M. Bianchi, Q. Zhou, and T. Illangasekare (2014b), A Connectivity-Based Modeling Approach for Representing Hysteresis in Macroscopic Two-Phase Flow Properties. *Energy Procedia*, 63, 3456-3463.

Cui, X., A. M. M. Bustin, and R. M. Bustin, (2009), Measurements of gas permeability and diffusivity of tight reservoir rocks: different approaches and their applications, *Geofluids* 9, 208-223.

Cupelli, C., B. Henrich, T. Glatzel, R. Zengerle, M. Moseler and M. Santer, (2008), Dynamic capillary wetting studied with dissipative particle dynamics, *New J. Phys*., 10, 043009.

Dosunmu, A., and E. E. Okoro (2012), Determination of moisture adsorption isotherm of shale from Agbada Formation using GAB model, *Res. J Eng. Sci*. 1, 27-33.

Downs, R. T., and M. Hall-Wallace (2003), The American mineralogist crystal structure database, *Am. Mineral.*, *88*(1), 247-250.

Elgmati, M., H. Zhang, B. Bai, R. Flori, (2011), Submicron-pore characterization of shale gas plays, *SPE North American Unconventional Gas Conference, The Woodlands, TX, June 14-16, 2011*. SPE 144050.

Emmanuel, O. E., and A. Dosunmu (2014), Experimental analysis of shale for evaluating shale drilling fluid interaction in Agbada Formation, *Brit. J. Appl. Sci. Technol*. 4, 4878-4907.

Espanol, P. and P.Warren, (1995), Statistical Mechanics of Dissipative Particle Dynamics, *Europhys. Lett*., 30, 191–196.

Fuchslin, R. M., H. Fellerman, A. Eriksson, and H.-J. Ziock, (2009), Coarse graining and scaling in dissipative particle dynamics, *J. Chem. Phys*, 130.

Ghanizadeh, A., S. Bhowmik, O. Haeri-Ardakani, H. Sanei, C. R. Clarkson, (2015), A comparison of shale permeability coefficients derived using multiple non-steady-state measurement techniques: Examples from Duvernay Formation, Alberta (Canada), *Fuel,* 140, 371-387.

Ghoufi, A., J. Emile and P. Malfreyt, (2013), Recent Advances in Many Body Dissipative Particles Dynamics Simulations of Liquid-Vapor Interfaces, *Eur. Phys. J. E: Soft Matter Biol. Phys*., 36, 10.

Goggins, D.J., R.L. Thrasher, and L.W. Lake (1988), A theoretical and experimental analysis of minipermeameter response including gas slippage and high velocity flow effects, *In Situ*, 12, 79-116.

Green, W.H., and G.A. Ampt (1911), Studies on soil physics, part 1, The flow of air and water through soils, *J. Agric. Sci*., 4, 1-24.

Greenspan, L., (1977), Humidity Fixed Points of Binary Saturated Aqueous Solutions, *J. Res. National Bureau Standards*, 81A (1), 89-96.

Groot, R. D. and P. B. Warren, (1997) Dissipative Particle Dynamics: Bridging the Gap between Atomistic and Mesoscopic Simulation, *J. Chem. Phys*., 1997, 107, 4423–4435

Henrich, B., C. Cupelli, M. Moseler, and M. Santer, (2007), An adhesive DPD wall model for dynamic wetting, A Letters Journal Exploring The Frontiers of Physics.

Hoogerbrugge, P. J. and J. M. V. A. Koelman, (1992), Simulating Microscopic Hydrodynamic Phenomena with Dissipative Particle Dynamics, *Europhys. Lett*., 19, 155–160.

Irving, J. H., and J. G. Kirkwood, (1950), *J. Chem. Phys*., 18, 817-829

Jones, S.C. (1987), Using the inertial coefficient, b, to characterize heterogeneity in reservoir rock, SPE 16949, *62nd Annual Technical Conference*, SPE, Dallas, September 27-30, 1987.

Kao, C.S., and J.R. Hunt (1996), Prediction of wetting front movement during one-dimensional infiltration into soils, *Water Resour. Res*., 32, 55-64.

Lucas, R. (1918) Ueber das zeitgesetz des kapillaren aufstiegs von flussigkeiten, *Kolloid Z*., 23, 15-18.

Luffel, D. L., and F. K. Guidry, (1992), New core analysis methods for measuring reservoir rock properties of Devonian Shale, *J. Petrol. Technol*., 1184-1190.

Luffel, D. L., C. W. Hopkins, P. O. Schetter Jr., (1993), Skeletal permeability measurement of gas productive shales, Paper SPE 26633, *68th Annual Technical Conference SPE*, Houston, TX October 3-3, 1993.

Luffel, D. L., (1993), Advances in Shale Core Analyses, Topical Report, June 1993, for Gas Research Institute.

Marsh, C. A., C. Backx, and M. H. Ernst, (1997), Static and Dynamic Properties of Dissipative Particle Dynamics, *Physical Review E*, 56 (2).

Philip, J.R. (1957), The theory of infiltration, 4, Sorptivity and algebraic infiltration equations, *Soil Sci*., 84, 257-264.

Profice, S., D. Lasseux, Y. Jannot, N. Jebara, and G. Hamon (2012), Permeability, porosity and Klinkenberg coefficient determination on crushed porous media, *Petrophysics*, 53, 430-438.

Roychaudhuri, R., T.T. Tsotsis, K. Jessen (2013), An experimental investigation of spontaneous imbibition in gas shales. *J. Petrol. Sci. Eng*. 111, 87-97.

Sposito, G., (1984), The Surface Chemistry of Soils, Oxford University Press, New York.

Suarez-Rivera, R., M. Chertov, D. Willberg, S. Green, J. Keller (2012), Understanding permeability measurements in tight shales promotes enhanced determination of reservoir quality. SPE 162816, *SPE Canadian Unconventional Resources Conference*, Calgary, October 30, 2012.

Supple, S., and N. Quirke, (2004), Molecular dynamics of transient oil flows in nanopores I: Imbibition speeds for single wall carbon nanotubes, *Journal of Chemical Physics*, 121, 8571-8579.

Tanikawa, W., and T. Shimamoto (2009). Comparison of Klinkenberg-corrected gas permeability and water permeability in sedimentary rocks, *Int. J. of Rock Mech*., 46, 229-238.

TICORA (2005), Final Report Reservoir Property Analysis, Woodford/Caney Shale, 21 pp, TICORA Geosciences, Inc., Arvada, Colorado.

Tokunaga, T.K., and J. Wan (2001), Surface-zone flow along unsaturated rock fractures, *Water Resour. Res*., 37, 287-296.

Tokunaga, T. K., K. R. Olson, and J. Wan, (2003), Moisture characteristics of Hanford gravels: Bulk, grain-surface, and intragranular components, *Vadose Zone J*, 2, 322-329.

Walker-Milani, Margaret E., (2011), Lithostratigraphy and petrophysics of the Middle Devonian Marcellus Shale in West Virginia and adjacent states. Master of Science thesis, West Virginia University, Department of Geology and Geography, Morgantown, West Virginia.

Washburn, E.W. (1921), The dynamics of capillary flow, *Physical Review*, 17(3), 273-283.

Warren, P. B., (2003), Vapor-liquid coexistence in many-body dissipative particle dynamics, *Physical Review E*, 68, 066702.